Journal of Power Sources 240 (2013) 122–130

Contents lists available at SciVerse ScienceDirect

Journal of Power Sources

journal homepage: www.elsevier.com/locate/jpowsour

Surface modification of commercial PtRu nanoparticles for methanol electro-oxidation

Che-Wei Kuo [a], I-Te Lu [a], Li-Chung Chang [a], Yu-Chi Hsieh [b], Yuan-Chieh Tseng [b], Pu-Wei Wu [b,*], Jyh-Fu Lee [c]

[a] Graduate Program for Science and Technology of Accelerator Light Source, National Chiao Tung University, Hsin-chu 300, Taiwan, ROC
[b] Department of Materials Science and Engineering, National Chiao Tung University, Hsin-chu 300, Taiwan, ROC
[c] National Synchrotron Radiation Research Center, Hsin-chu 300, Taiwan, ROC

HIGHLIGHTS

- Surface modification on commercially available PtRu nanoparticles to render a Pt-rich surface.
- A displacement reaction between Ru atoms on the PtRu nanoparticles and Pt ions in an aqueous hexachloroplatinic acid solution.
- Deliberate control over the severity of displacement reaction leads to a significant increment in mass activity for methanol electro-oxidation.

ARTICLE INFO

Article history:
Received 1 February 2013
Received in revised form
1 April 2013
Accepted 1 April 2013
Available online 6 April 2013

Keywords:
Platinum
Ruthenium
Displacement reaction
Methanol electro-oxidation
X-ray absorption spectroscopy

ABSTRACT

The surfaces of commercially available PtRu nanoparticles (PtRu/C) have been successfully modified via a displacement reaction between the Ru atoms on the PtRu/C and the Pt ions in an aqueous hexachloroplatinic acid solution. The concentration of the hexachloroplatinic acid solution was deliberately formulated to allow for the formation of sub-monolayered Pt (Pt(1/16)) and monolayered Pt (Pt(1/8)) on the surface of PtRu/C. Material characterization, including X-ray diffraction patterns and transmission electron microscopy images, showed that the PtRu phases of the samples were identical but that the particle sizes increased slightly after the surface modification. Data from inductively coupled plasma mass spectrometry confirmed the deposition of Pt with negligible loss of Ru. X-ray absorption spectroscopy showed Pt-enriched surfaces, and the surface Pt content decreased in the order Pt(1/8) > Pt(1/16) > PtRu/C. Cyclic voltammetry and chronoamperometry were conducted for methanol electro-oxidation, and our results indicated impressive catalytic ability and carbon monoxide tolerance for Pt(1/16), followed by Pt(1/8) and PtRu/C. The mass activities of Pt(1/16) and Pt(1/8) increased 223% and 135% over that of PtRu/C. We attributed the observed improvements to the reduced amount of Ru on the PtRu surface, which resulted in an optimized PtRu ratio with enhanced catalytic ability.

1. Introduction

The development of clean and affordable energy is critically important because of dwindling oil supplies and harmful carbon dioxide emissions. Among numerous technologies under study, the direct methanol fuel cell (DMFC) has recently attracted considerable attention as a promising power source for portable electronics [1–4]. The operation of a DMFC entails the oxidation of methanol in an acidic electrolyte to produce electricity along with carbon dioxide and water. The dehydrogenation of methanol is intrinsically slow because the intermediate product, carbon monoxide, is known to adsorb strongly onto the Pt sites of the catalysts, thereby inhibiting their catalytic functions. Therefore, a secondary element alloyed with Pt to promote the oxidation of carbon monoxide so that the methanol electro-oxidation (MOR) process can proceed. Among the numerous candidates under scrutiny, the PtRu alloy has demonstrated impressive electrocatalytic ability and durability [5–7]. The Ru facilitates the oxidative removal of carbon monoxide via mechanisms that involve electronic effects and a bifunctional model [8,9].

Electrocatalysis is an interfacial phenomenon in which the surface composition, the structure, and the morphology of a catalyst play significant roles in determining its catalytic performance. In particular, to increase the catalyst utilization rate and reduce costs,

* Corresponding author. Tel.: +886 3 5131227; fax: +886 3 5724727.
E-mail address: ppwu@mail.nctu.edu.tw (P.-W. Wu).

0378-7753/$ – see front matter © 2013 Elsevier B.V. All rights reserved.
http://dx.doi.org/10.1016/j.jpowsour.2013.04.001

current research has been focused on the synthesis of core–shell nanoparticles that provide better activity and durability [10,11]. In the literature, a variety of surface modification schemes for PtRu nanoparticles have been explored with various degrees of success. Those techniques have included electroplating, copper under potential deposition, heat treatments, dealloying, displacement reactions, the use of colloidal precursors, etc. [12–17]. Among these techniques, a displacement reaction is considered to be the simplest because it is a spontaneous reaction that does not require external stimuli. Because of the difference between the redox potentials of Pt and Ru, when PtRu nanoparticles are immersed in an electrolyte that contains Pt ions, the Ru atoms on the surface are oxidized, thereby releasing electrons to reduce Pt ions from the electrolyte and, leading to a PtRu surface enriched with Pt. This process was found to be important in our previous study of the pulse deposition of PtRu nanoparticles, where the Ru was alternately deposited and oxidized during current-on time (T_{on}) and current-off time (T_{off}), whereas Pt was deposited continuously [18]. Hence, PtRu nanoparticles with compositions that ranged from $Pt_{50}Ru_{50}$ to $Pt_{90}Ru_{10}$ could be fabricated through a simple adjustment of the duty cycle ($T_{on}/(T_{on} + T_{off})$) in a single pulse.

In a displacement reaction between Ru and Pt, the Ru atoms can release electrons to reduce Pt ions through two possible routes; corrosive dissolution and a cementation reaction [19,20]. The corrosive dissolution is a straightforward electrochemical oxidation process that results in Ru cations in the electrolyte. However, the cementation reaction is a surface oxidation step in which the Ru atoms become oxyhydroxides, $Ru(OH)_x$, without leaving the Ru surface. Our group has previously employed X-ray absorption spectroscopy (XAS) to investigate the surface PtRu arrangements in details by immersing Ru nanoparticles in Pt baths with various pH levels. Because the acidity determines the solvating ligands, which, in turn, varies the respective redox potentials of Pt and Ru, the severity of the displacement reaction is therefore altered, thereby engendering distinct surface Pt/Ru ratios and MOR activities as a consequence [21]. This study provides direct evidence of the fine-tuning of the PtRu surface composition via a displacement reaction.

Modifications of the surfaces of commercially available PtRu nanoparticles have been reported by Hwang et al. and Li et al., who were attempting to optimize the PtRu ratios in PtRu alloys to further enhance their MOR activities [22,23]. However, they employed heat treatments, which are often time-consuming. In this work, we used the displacement reaction route because of its simplicity. In addition, the difference in redox potentials is affected by the concentration of Pt ions according to the Nernst equation, and the number of Pt ions in the electrolyte was deliberately formulated to allow for the formation of sub-monolayered and monolayered Pt on the PtRu surface after deposition. Detailed analysis was performed to characterize the structural evolution of the PtRu after the displacement reaction, and this structural information was correlated to the electrochemical MOR measurements.

2. Experimental

2.1. Sample preparation

As-received carbon-supported PtRu (E-TEK, 40 wt%) nanoparticles (PtRu/C) were heat-treated under a mixture of H_2 and Ar (1:1 vol. ratio) at a heating rate of 3 °C min^{-1} and were maintained at 300 °C for 1 h to remove surface oxides and contaminants. After cooling to 25 °C, the PtRu/C nanoparticles were suspended in an aqueous hexachloroplatinic acid (H_2PtCl_6; 99.9 wt%) solution in a two-neck round-bottom distillation flask. The molar ratio between the Pt ions in the hexachloroplatinic acid and the suspended PtRu/C nanoparticles was adjusted to 1/16 or 1/8. These ratios were selected because they allow the formation of sub-monolayered (1/16) and monolayered (1/8) Pt on the PtRu surface if all Pt ions are assumed to be successfully reduced. The resulting surface-modified PtRu/C nanoparticles were labeled as Pt(1/16) and Pt(1/8), respectively. The hexachloroplatinic acid solution was pre-purged with Ar for 20 min to remove dissolved oxygen. To accelerate the displacement reaction after the PtRu/C was immersed in the hexachloroplatinic acid solution, the mixture was heated in an oil bath at 100 °C and was subjected to a distillation reflow under an Ar atmosphere for 90 min. The surface-modified samples, Pt(1/16) and Pt(1/8), were filtered and rinsed thoroughly with de-ionized water.

2.2. Materials characterization

X-ray diffraction (XRD) patterns were obtained on a Bruker D2 Phaser equipped with a Cu Kα radiation source ($\lambda = 1.54$ Å) to identify relevant phases in the samples. The X-ray diffractograms were recorded at a scan rate of 0.1 °s^{-1} for 2θ values between 5° and 90°. A transmission electron microscope (TEM; Philips TECNAI 20) was used to observe the morphologies and sizes of the samples. The exact amounts of Pt and Ru, as well as their molar ratios, before and after the displacement reaction, were determined using an inductively coupled plasma mass spectrometer (ICP-MS; Agilent 7500CE).

X-ray absorption spectroscopy (XAS) for the Pt L_{III}-edge (11,564 eV) and the Ru K-edge (22,117 eV) was conducted at beam lines of BL01C1 and BL17C1, respectively, at the Taiwan Light Source, National Synchrotron Radiation Research Center (NSRRC), Hsinchu, Taiwan. The 1.5 GeV storage-ring energy was operated with a top-up storage current of 360 mA. A double crystal monochromator constructed of (111) Si was used for energy selection with a resolution ($\Delta E/E$) better than 2×10^{-4} at both beam lines. Rhodium- or Pt-coated mirrors were used to reject high-order harmonics and to, collimate (upstream), and refocus (downstream) the X-ray beam. The XAS measurements were performed in fluorescence detection mode at 25 °C. A Lytle fluorescence detector along with three gas-filled ionization chambers were used to record the intensities of the X-ray fluorescence photons from the sample, the incident beam, the transmitted beam, and the beam transmitted through the reference sample. Platinum foil and H_2PtCl_6 electrolyte, and Ru and RuO_2 powders served as reference materials for the Pt L_{III}-edge and Ru K-edge measurements, respectively.

Extended X-ray absorption fine structure (EXAFS) data analysis and fitting were processed using the IFEFFIT 1.2.11c data analysis software package (Athena, Artemis, and FEFF6). The recorded profiles were calibrated by being aligned against the reference materials in each scan. Subsequently, those profiles were averaged to achieve better signal quality. X-ray absorption near edge structure (XANES) spectra were acquired after normalization using the Athena software. Pre/post-edge background subtractions and normalization with respect to the edge jump were performed to obtain the EXAFS function using standard protocols. The resulting EXAFS function, χ(E), was transformed from energy space to *k*-space. In the high *k*-region of χ(*k*) data, multiplication by k^3 was applied to compensate for the damping of EXAFS oscillations. Then, the k^3-weighted χ(*k*) data were Fourier-transformed to *r*-space. The selected specific ranges in *k*-space for the Fourier transformation were 3.32–12.74 $Å^{-1}$ for the Pt L_{III}-edge and 4.01 to 13.42 $Å^{-1}$ for the Ru K-edge. The EXAFS curve fitting in *r*-space was applied using a nonlinear least-squares algorithm. The ranges of *r*-space for the curve fitting were established, without phase correction, from 1.90 to 3.17 Å for Pt and from 1.70 to 2.73 Å for Ru. Relevant structural characteristics were fitted using the Artemis software package with

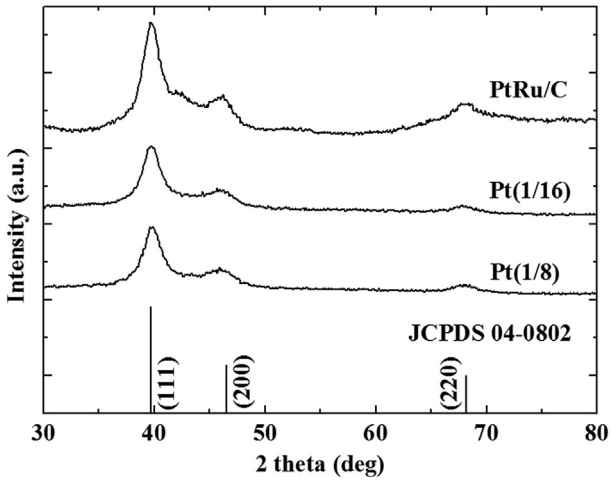

Fig. 1. The XRD diffraction patterns for PtRu/C, Pt(1/16), and Pt(1/8), as well as the pattern of Pt from JCPDS 04-0802 as a reference.

theoretical standards generated by FEFF6 code. The fitting parameters included the coordination number (N), the bond distance (R), the Debye–Waller factor ($\Delta\sigma_j^2$), and the inner potential shift (ΔE_0).

2.3. Electrochemical analysis

To prepare working electrodes, the samples were re-dispersed in de-ionized water and the dispersion was deposited onto a rotating-disc electrode (RDE) using a micro pipette with a capacity of 25 μL. For the preparation of the dispersion, 3.6 mg of the sample in 1.8 mL of a solution that contained de-ionized water and 2 μL of Nafion ionomer solution (5 wt%, Sigma–Aldrich) as a binder. Cyclic voltammetry (CV) scans were performed between −0.2 and 0.7 V at 50 mV s^{-1} in 500 mL of 0.1 M $HClO_4$ aqueous solution. The integrated charge associated with hydrogen desorption was estimated to obtain the electrochemical surface area (ECSA). For MOR measurements, multiple CV scans were performed between −0.2 and 0.9 V at 20 mV s^{-1} in a 500 mL aqueous solution of 0.5 M H_2SO_4 and 1 M CH_3OH. To evaluate life time performance against CO poisoning, chronoamperograms were obtained at 0.4 V for 1 h in 500 mL of an aqueous solution of 0.5 M H_2SO_4 and 1 M CH_3OH. Prior to each electrochemical analysis, the electrolyte was pre-purged with Ar for 20 min to remove dissolved oxygen. The area for the working electrode, RDE, was 0.196 cm^2, and the RDE was stationary throughout the entire experiment. A Ag/AgCl electrode and Pt foil (10 cm^2) were used as the reference and counter electrodes, respectively. The electrochemical measurements were performed at 25 °C in a three-electrode arrangement using a Solartron 1287A electrochemical interface.

3. Results and discussion

XRD patterns for PtRu/C, Pt(1/16), and Pt(1/8) are displayed in Fig. 1, along with the pattern of standard Pt according to JCPDS (04-0802) for reference purpose. According to the JCPDS data, the Pt exists in a fcc phase with (111), (200), and (220) diffraction signals located at 39.76, 46.24, and 67.45°, respectively. Because the atomic radius of Ru is smaller than that of Pt, the alloying of Ru into the fcc Pt structure is expected to result in a smaller unit cell which leads to a slight shift of diffraction peaks to larger angles. Indeed, the (111), (200), and (220) diffraction peaks for PtRu/C were recorded at 40.22, 46.66, and 68.76°, respectively. Interestingly, after surface modification, relevant diffraction signals appeared at identical positions in both the Pt(1/16) and Pt(1/8) cases. These results suggested that the displacement reaction that occurred between Pt ions in the electrolyte and the Ru atoms in the PtRu/C nanoparticles induced a structural/compositional alteration predominately on the surface, whereas the bulk of the PtRu nanoparticles remained intact. Using Scherrer's equation and the (220) diffraction peak, we calculated the crystal size for the PtRu/C to be 3.06 nm. After surface modification, the crystal sizes became slightly larger: 3.3 and 3.45 nm for the Pt(1/16) and Pt(1/8) samples, respectively. These findings indicated that a higher concentration of Pt ions engendered a stronger displacement reaction for the deposition of additional Pt, which resulted in a larger PtRu particle size. However, the amount of Pt deposited was still insufficient to manifest itself in the XRD pattern as diffraction signals of pure Pt.

Fig. 2 presents the TEM images of PtRu/C, Pt(1/16), and Pt(1/8). Apparently, before and after the surface modification, the PtRu nanoparticles exhibited moderate agglomeration. For each sample, the particle sizes determined using the TEM imaging software were slightly larger than those estimated using Scherrer's equation with the (220) diffraction peak. For example, the average nanoparticle sizes were 3.12 ± 1.56, 3.62 ± 2.66, and 3.89 ± 2.41 nm for PtRu/C, Pt(1/16), and Pt(1/8), respectively. We surmised that these larger sizes were possibly caused by localized agglomeration among individual nanoparticles which rendered them indistinguishable by TEM.

During the surface modification treatment, the Pt ions in the electrolyte and the Ru atoms in the PtRu nanoparticles engaged in a displacement reaction in which the Pt ions were reduced while the Ru atoms suffered from either corrosive dissolution or a surface oxidation process (i.e., a cementation reaction). Consequently, considerable variations in both the surface composition and the

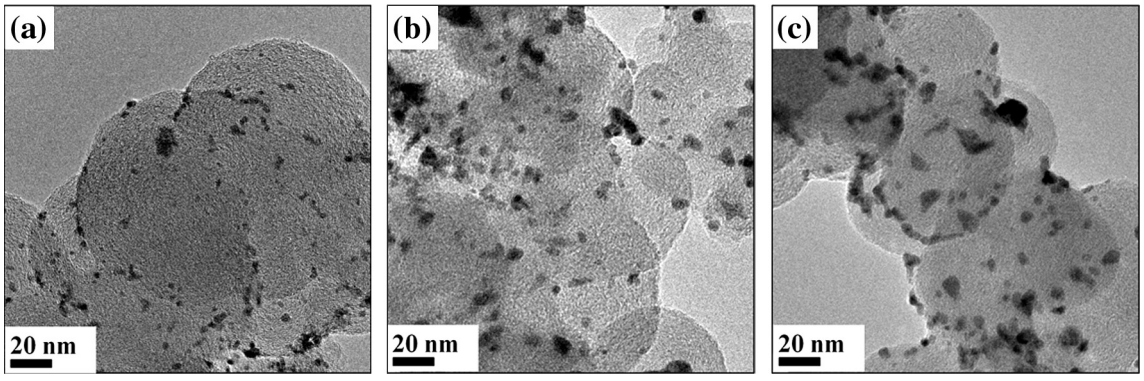

Fig. 2. The TEM images for (a) PtRu/C, (b) Pt(1/16), and (c) Pt(1/8).

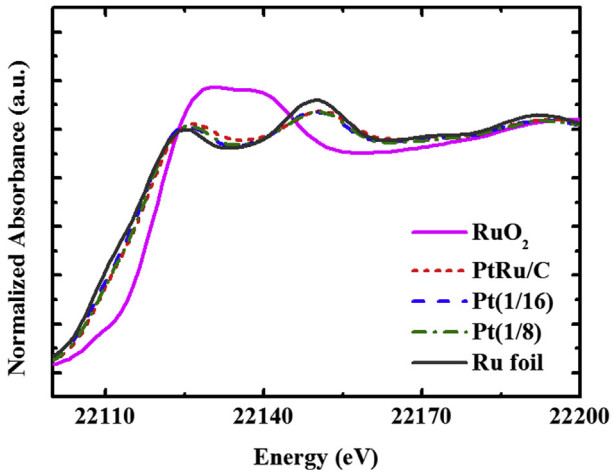

Fig. 3. The Ru K-edge XANES spectra for PtRu/C, Pt(1/16), and Pt(1/8), as well as those of Ru and RuO_2, which served as reference materials.

bonding arrangements for the surface-modified samples were expected, and the information could be qualitatively acquired from XAS spectra. Fig. 3 shows the Ru K-edge XANES spectra for PtRu/C, Pt(1/8), Pt(1/16), Ru metal, and RuO_2. For the K-edge absorption curves, an oxidized state would result in a peak shifted toward higher energy. As shown, the spectrum of Ru metal showed an absorption peak at 22,117.2 eV, whereas the RuO_2 exhibited a higher-energy absorption peak at 22,120.9 eV because of its +4 charge. Among our samples, the PtRu/C, Pt(1/16), and Pt(1/8) exhibited absorption peaks at 22,118.1, 22,117.2, and 22,117.4 eV, respectively. These absorption curves were rather close to that of metallic Ru, thereby confirming their metallic natures. Stoupin et al. and Viswanathan et al. have demonstrated identical phenomena in their XAS studies on PtRu nanoparticles [24,25].

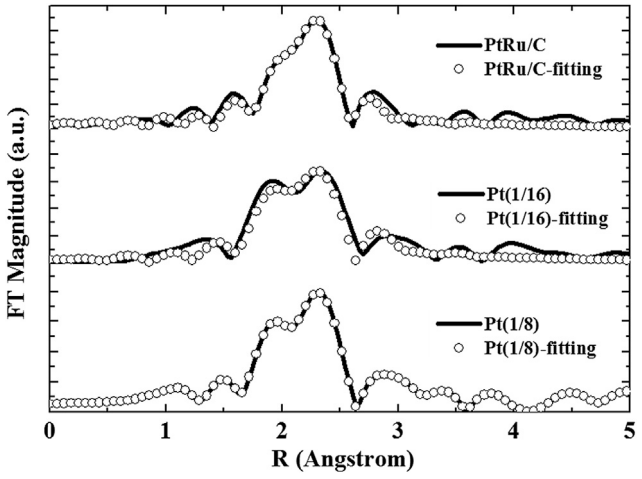

Fig. 4. The Ru K-edge Fourier-transformed EXAFS spectra and their respective fitting results for PtRu/C, Pt(1/16), and Pt(1/8) from Fig. 3.

The Ru K-edge Fourier-transformed EXAFS spectra for PtRu/C, Pt(1/16), and Pt(1/8) are shown in Fig. 4. The peaks at 1.9 Å and 2.3 Å (without phase correction) were associated with Ru–Ru bonds and Ru–Pt bonds, respectively. The EXAFS fitting results are summarized in Table 1. As listed in the table, the coordination number of Ru–Ru (N) was approximately 3.2–3.54, which suggested that the Ru–Ru bonding arrangement remained mostly unaltered before and after the surface modification. In contrast, a considerable increase in the coordination number of Ru–Pt was observed, with values of 5.27, 6.8, and 7.22, for PtRu/C, Pt(1/16), and Pt(1/8), respectively. We hypothesized that during the displacement reaction, the Ru–Ru bond remained relatively intact due to limited loss of Ru from corrosive dissolution. However, on the surface where the displacement reaction was vigorous, excess Pt deposition was expected, which would lead to increased Pt–Ru bond coordination numbers, with the extent of the increase being proportional to the severity of the displacement reaction. In addition to a numerical approach, a qualitative confirmation about the bonding arrangements can be achieved through observation of the evolution of the line shapes in the EXAFS spectra. For example, the most notable change in the EXAFS line-shape was the emergence of the shoulder at 1.9 Å after the displacement reaction, which can be directly linked to the emergent Ru–Pt bond in the first atomic shell, in agreement with the calculated results (open squares in Fig. 4).

The oxidation state for Pt atoms was determined from the Pt L_{III}-edge absorption peak, and the resulting XANES spectra are given in Fig. 5. For L-edge absorption, a greater oxidation state usually features a greater white line intensity, as a result of more unoccupied states allowing the photo-excitation process. Here, the metallic Pt exhibited the lowest white line intensity, whereas the greatest intensity was obtained with the H_2PtCl_6. However, the white line intensities for PtRu/C, Pt(1/16), and Pt(1/8) were very similar, and were all close to that of Pt metal. In general, the Pt atoms in these samples should remain metallic; however their white-line intensities were slightly greater than that of a pure Pt. The difference in white-line intensities is likely due to the increased number of d-band states with Ru–Pt orbital hybridization, as has been reported previously [24–27]. We also note that the electronic modifications induced by the Ru–Pt hybridization caused both Pt and Ru to exhibit oxidation states slightly greater than those of their metallic counterparts, whereas such modifications appeared to affect their catalytic abilities to only a small extent, as will be discussed later.

Fig. 6 provides the Pt L_{III}-edge Fourier-transformed EXAFS spectra for PtRu/C, Pt(1/16), and Pt(1/8). The peaks located at 2.1 Å and 2.7 Å (without phase correction) corresponded to the Pt–Ru bond and Pt–Pt bond, respectively. Relevant fitting parameters are listed in Table 2. The Pt L_{III}-edge EXAFS fitting results indicated that the coordination number of the Pt–Ru bonds in PtRu/C, Pt(1/16),

Table 1
EXAFS fitting parameters at the Ru K-edge for PtRu/C, Pt(1/16), and Pt(1/8), respectively.

	Path	Coordination number, N	$P_{Ru} \cdot N_{Ru-Pt}/N_{Total}$	Bond distance, R (Å)	Inner potential shift, ΔE_0 (eV)	Debye–Waller factor, $\Delta\sigma_j^2$ ($\times 10^{-3}$ Å^2)
PtRu/C	Ru–Ru	3.54	59.8%	2.65	−11.28	5.78
	Ru–Pt	5.27		2.71	−7.55	11.15
Pt(1/16)	Ru–Ru	3.20	68.0%	2.64	−14.01	5.50
	Ru–Pt	6.80		2.71	−6.81	14.43
Pt(1/8)	Ru–Ru	3.29	68.7%	2.64	−12.70	5.33
	Ru–Pt	7.22		2.70	−8.20	14.36

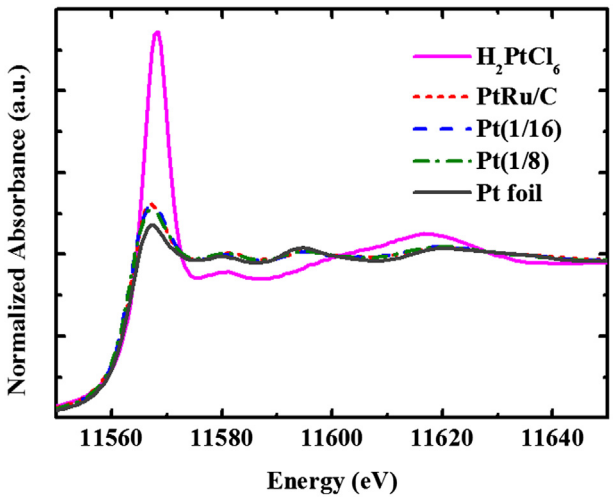

Fig. 5. The Pt L_{III}-edge XANES spectra for PtRu/C, Pt(1/16), and Pt(1/8), as well as those for Pt foil and H_2PtCl_6 electrolyte, which served as reference materials.

and Pt(1/8) was 1.96, 1.83, and 1.59, respectively. The modest decrease in the Pt–Ru coordination number can be attributed to the displacement reaction because, the number of Pt atoms on the surface increases, the average coordination number of the Pt–Ru bonds would decrease accordingly. However, the Pt–Pt coordination numbers for PtRu/C, Pt(1/16), and Pt(1/8) were 3.44, 4.69, and 5.71, respectively, thereby revealing that the number of Pt–Pt bonds increased as the severity of the displacement reaction

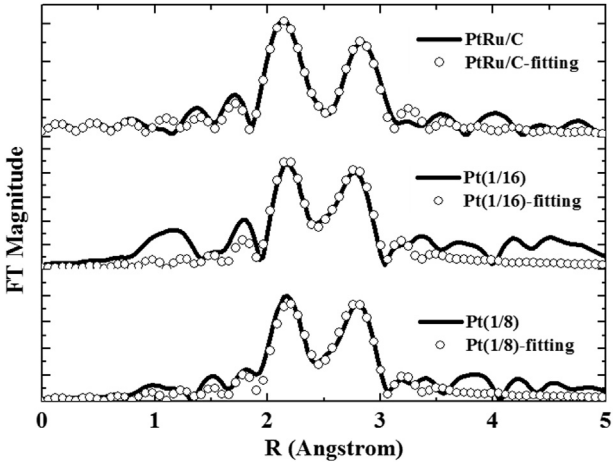

Fig. 6. The Pt L_{III}-edge Fourier-transformed EXAFS spectra and their respective fitting results for PtRu/C, Pt(1/16), and Pt(1/8) from Fig. 5.

Table 3
Results from material characterizations for PtRu/C, Pt(1/16), and Pt(1/8), respectively.

	Pt loading (μg)[a]	Ru loading (μg)[a]	PtRu atomic ratio	Particle diameter	
				(nm)[b]	(nm)[c]
PtRu/C	63.32	33.01	0.99	3.06	3.12 (1.56)
Pt(1/16)	72.19	31.48	1.19	3.30	3.62 (2.66)
Pt(1/8)	77.68	32.27	1.25	3.45	3.89 (2.41)

[a] From ICP-MS.
[b] From XRD Pt (220) diffraction peak.
[c] From TEM imaging software and standard deviation (σ) is provided in bracket.

increased. Hence, the ratio between the Pt–Ru bonds and the total number of bonds, labeled as P_{Pt} in Table 2, decreased from 36.3% for PtRu/C, to 28.1% for Pt(1/16), and 21.8% for Pt(1/8). Notably, according to the results in Table 1, the total coordination numbers (i.e., the sum of the coordination numbers for Ru–Ru and Ru–Pt) for Ru were 8.8, 10, and 10.4 for PtRu/C, Pt(1/16), and Pt(1/8), respectively. In contrast, from the results in Table 2, the total coordination numbers (i.e., the sum of the coordination numbers for Pt–Ru and Pt–Pt) for Pt were 5.4, 6.5, and 7.3 for PtRu/C, Pt(1/16), and Pt(1/8), respectively. The authors of previous XAS studies on binary nanoparticles [28], have noted that the atoms that reside predominantly on the surface are expected to have fewer total bonding neighbors because of terminated coordination on the surface. Therefore, we can reasonably conclude that in our samples, the Pt is relatively-rich on the surface because of its fewer bonding neighbors compared to those of Ru.

The quantitative results from ICP-MS, as well as the crystal sizes determined by XRD and TEM are presented in Table 3. As expected, the atomic ratio (Pt/Ru) in the as-received PtRu/C was close to 1. In contrast, the Pt/Ru ratios in Pt(1/16) and Pt(1/8) were 1.19 and 1.25, respectively. Apparently, the loss of Ru during the displacement reaction was negligible despite a substantial increase in the Pt mass for both Pt(1/16) and Pt(1/8). Hence, we realized that the corrosive dissolution of Ru was not responsible for the reduction of Pt ions in the electrolyte. The pH values of the Pt(1/16) and Pt(1/8) solutions were 2.6 and 2.3, respectively. According to the Pourbaix diagram, the Ru in PtRu is expected to maintain its metallic state under such acidic environments [29], which is consistent with our finding of insignificant mass loss due to corrosive dissolution. Consistent results were also recorded in similar studies in which a minute amount of Ru was found to undergo corrosive dissolution in a bath with a pH of 1, whereas the majority of Ru underwent cementation transformation to $Ru(OH)_x$ [21,30]. Moreover, the oxidative dissolution of Ru has been suggested to occur at a potential more positive than the equilibrium potential of Pt/$[PtCl_6]^{2-}$; as such, it is unlikely to trigger the displacement reaction [31].

In our case, the Ru atoms are oxidized, thereby forming $Ru(OH)_x$ on the surface while the Pt ions are simultaneously reduced. According to Brankovic et al. [19], the driving force (ΔU) for the

Table 2
EXAFS fitting parameters at the Pt L_{III}-edge for PtRu/C, Pt(1/16), and Pt(1/8), respectively.

	Path	Coordination number, N	$P_{Pt} \cdot N_{Pt-Ru}/N_{Total}$	Bond distance, R (Å)	Inner potential shift, ΔE_0 (eV)	Debye–Waller factor, $\Delta\sigma_j^2$ ($\times 10^{-3}$ Å^2)
PtRu/C	Pt–Ru	1.96	36.3%	2.71	4.45	4.82
	Pt–Pt	3.44		2.74	5.68	4.73
Pt(1/16)	Pt–Ru	1.83	28.1%	2.71	5.74	4.37
	Pt–Pt	4.69		2.74	7.20	5.31
Pt(1/8)	Pt–Ru	1.59	21.8%	2.70	6.20	3.12
	Pt–Pt	5.71		2.72	5.17	6.07

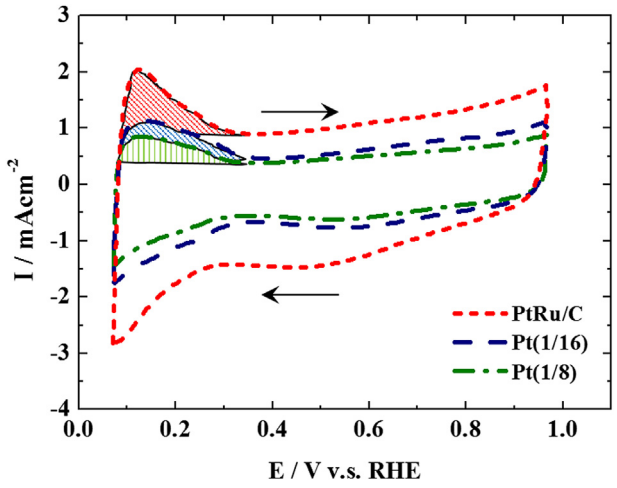

Fig. 7. The CV profiles of samples in 0.1 M $HClO_4$ aqueous solutions; the profiles were used to determine the ECSA for PtRu/C, Pt(1/16), and Pt(1/8). The highlighted area was used to estimate the ECSA.

displacement reaction is the potential difference between the $[PtCl_6]^{2-}$ reduction and the Ru oxidation, as shown in Eqs. (1)–(4). Compared with Pt(1/16), Pt(1/8) incurred a stronger displacement reaction, which led to increased Pt deposits, a higher Pt/Ru ratio, and a larger nanoparticle size because of its greater Pt concentration.

$$Ru^0 + x(H_2O) = RuO_xH_y + (2x - y)H^+ + (2x - y)e^- \quad (1)$$

$$[PtCl_6]^{2-} + 4e^- = Pt^0 + 6Cl^- \quad (2)$$

$$\Delta U = \Delta E_{Pt/PtCl_6^{2-}} - \Delta E_{Ru^0/Ru_{oxidized}} > 0 \quad (3)$$

$$\left(\Delta E[V] \sim 0.74 + 0.015 \log[PtCl_6]^{2-}\right) \quad (4)$$

According to previous studies on PtRu nanoparticles by Hwang et al. and Huang et al., Pt and Ru exhibit distinct affinity toward oxygen (air) and hydrogen [22,32]. For example, a hydrogen treatment on PtRu nanoparticles encourages the out-diffusion of Pt, thereby rendering a Pt-rich surface. However, a heat treatment under an oxygen atmosphere induces the oxyphilic Ru to migrate outward so that a Ru-rich surface is formed. Because the as-received PtRu/C, in our case, was subjected to a hydrogen treatment, it was expected to exhibit a Pt-rich surface even before undergoing the surface modification process. Indeed, a reduced total bonding number of Pt was found in the PtRu/C. For the samples subjected to the surface modification, during which excess Pt was deposited, the surface of PtRu became further enriched with Pt.

Fig. 7 demonstrates the CV profiles of hydrogen adsorption/desorption for PtRu/C, Pt(1/16), and Pt(1/8). Because the pH value for the 0.1 M $HClO_4$ aqueous solution used for the ECSA measurement was 1.16, the potential for the reversible hydrogen electrode (RHE) became −0.268 V (vs. Ag/AgCl) because RHE = [−0.200 − 0.0591 × (pH)]. Hence, in our case, the potential window for the CV scans was 0.07–0.97 V (vs. RHE). To estimate the ECSA value, we selected the anodic peak in the potential window of 0.07–0.32 V (vs. RHE) and the area used to calculate the ECSA is highlighted in Fig. 7. It is understood that at a potential close to 0 V (vs. RHE), hydrogen evolution occurs, which interferes with the hydrogen adsorption/desorption behaviors. This interference leads to variations in the ECSA and to unreliable data. Therefore, the hydrogen adsorption/desorption experiments were necessarily performed at slightly positive potentials. Our method for determining ECSA is consistent with those previously reported in the literature. For example, Wang et al. used a 0.1 M $HClO_4$ aqueous solution to determine the ECSA at a starting potential of 0.05 V (vs. RHE) [33]. According to the ECSA values listed in Table 4, the ECSA values followed the order PtRu/C > Pt(1/16) > Pt(1/8). Because the sample weights were kept constant when the working electrodes were prepared, the number of nanoparticles deposited on the RDE decreased in the order PtRu/C > Pt(1/16) > Pt(1/8) because the PtRu/C exhibited the least mass per nanoparticle. Hence, the PtRu/C exhibited the largest ESCA value, as expected.

The results in Fig. 7 also indicate that the capacitive currents among our samples varied considerably. Indeed, for a single-component system such as Pt, the double-layer capacitance is affected by the fabrication methods involved; consequently, the resulting CV profiles should be similar among different samples and allow a fair comparison. However, in our case of PtRu binary nanoparticles, the Ru atoms are known to exhibit pseudocapacitive responses because the surface Ru atoms were converted into ruthenium oxides and oxyhydroxides, thereby allowing the intercalations and deintercalations of protons. Hence, the presence of excess Ru atoms on the PtRu surface resulted in an accordingly larger capacitive current. Similar behaviors have been reported by Iwasita et al., who studied various compositions of PtRu and observed substantially larger capacitive currents as the Ru content increased [34]. Even for a single-component Ru film, larger capacitive current responses have been observed, and their values were proportional to the amount of Ru on the electrodes [35]. In our case, the amount of Ru atoms on the PtRu nanoparticle surface follows the order of PtRu/C > Pt(1/16) > Pt(1/8). As a result, we recorded double-layer capacitances in an identical sequence because of the presence of surface Ru atoms.

Fig. 8 shows the MOR CV profiles with respect to the apparent current density and the mass activity of our samples. Because the

Table 4
Electrochemical parameters from CV scans for PtRu/C, Pt(1/16), and Pt(1/8), respectively.

Specimen	Anodic scan		Cathodic scan					
	V_a[a] (mV)	i_a[b] (mA mg_{Pt}^{-1})	V_c[c] (mV)	i_c[d] (mA mg_{Pt}^{-1})	V_{onset}[e] (mV)	ECSA[f] (cm^2)	ECSA[f] (cm^2 mg_{Pt}^{-1})	i_a/i_c
PtRu/C	885.2	137.7	718.4	107.6	678.1	2.46	38.9	1.28
Pt(1/16)	929.5	444.3	768.4	352.0	616.5	2.09	28.9	1.26
Pt(1/8)	921.1	323.3	757.8	254.7	639.5	1.34	17.7	1.27

[a] Potential at peak mass activity in anodic scan.
[b] Peak mass activity in anodic scan.
[c] Potential at peak mass activity in cathodic scan.
[d] Peak mass activity in cathodic scan.
[e] Onset potential in anodic scan.
[f] ECSA from hydrogen desorption data.

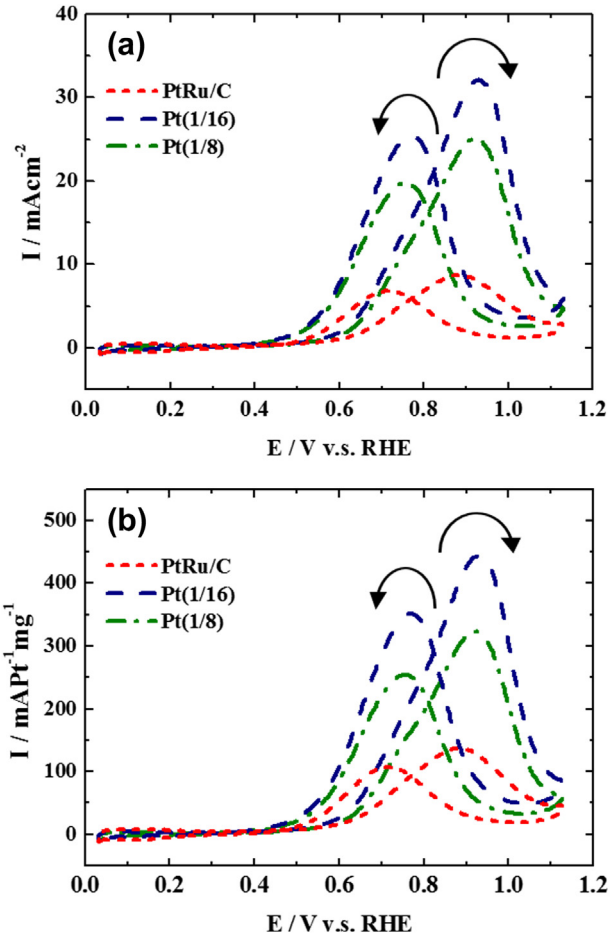

Fig. 8. The MOR CV profiles with respect to (a) the apparent current density and (b) the mass activity for PtRu/C, Pt(1/16), and Pt(1/8). The electrolyte is an aqueous solution of 0.5 M H_2SO_4 and 1 M CH_3OH.

pH value for the 0.5 M H_2SO_4 was 0.49, −0.229 V (vs. Ag/AgCl) became 0 V (vs. RHE) and the CV curves were plotted against RHE. Relevant parameters, including the onset potentials, the peak currents (i_a) and potentials (V_a) for anodic scans, the peak currents (i_c) and potentials (V_c) for cathodic scans, as well as the i_a/i_c ratio are also provided in Table 4. The i_a/i_c ratios reported in the literature reflect the capability of a catalyst material to remove CO after methanol dehydrogenation. As shown, these samples exhibited obvious anodic currents with relatively reduced cathodic currents, as indicated by their i_a/i_c values, which were consistently greater than 1. In our previous study of sputtering-derived Pt nanoparticles for MOR, the i_a/i_c ratio was only 0.88 because of severe carbon monoxide poisoning on the Pt surface [36]. These constant i_a/i_c ratios of 1.2 suggest that the Ru atoms were still present on the surface after the displacement reactions, albeit in smaller quantities. The onset potential could also be used as an indicator for MOR activity because a smaller onset potential is always desirable. Among our samples, the respective onset potentials for PtRu/C, Pt(1/16), and Pt(1/8) were 449.1, 387.5, and 410.5 mV. Moreover, the mass activities of the samples exhibited an identical pattern in the order Pt(1/16) > Pt(1/8) > PtRu/C. For example, the mass activities of PtRu/C, Pt(1/16), and Pt(1/8) were 137.7, 444.3, and 323.3 mA mg_{Pt}^{-1}, respectively, which amounts to a 221% improvement in the electrocatalytic ability for the Pt(1/16) compared to that of PtRu/C.

The enhancement in the MOR ability for Pt(1/16) can be rationalized by its PtRu composition on the surface. Electrocatalysis is a surface phenomenon; therefore, the surface atomic ratio is extremely critical, as opposed to the bulk composition. In the literature, evidence of desirable PtRu ratios at or near 1:1 has been proposed and verified experimentally [37,38]. However, some authors have suggested that the optimized ratio of surface Ru is merely 10% [39–41]. In addition, in their studies, a deterioration in MOR activities was observed when the amount of surface Ru deviated from the optimized 10% ratio. We hypothesize that, in our case, the Pt(1/16) allows the formation of residual Ru at a ratio of approximately 10%, whereas the Pt(1/8) contains additional deposited Pt and thus exhibits a surface Ru ratio less than 10%, thereby leading to its reduced MOR mass activity. However, the surface Ru content of the PtRu/C after the hydrogen treatment is still greater than 10%.

Fig. 9 shows the chronoamperograms for our samples at 0.4 V for 60 min, which reflect their mass activities. Apparently, the PtRu/C suffered from a severe current decay during the first 10 min, whereas both Pt(1/16) and Pt(1/8) were relatively stable with modest declines. In addition, the Pt(1/16) exhibited the largest mass activity, whereas the PtRu/C exhibited the smallest values among all of the measured samples. The loss of MOR activity was expected because poisonous intermediates were able to adsorb onto the Pt surface, thereby compromising its catalytic ability and, resulting in gradual current deterioration [42,43]. In our case, after showing superior MOR behavior for the Pt(1/16), the chronoamperogram again confirmed its superiority for MOR behavior with respect to life-time performance.

Notably, in Fig. 9, the PtRu/C exhibited a larger current compared to those of Pt(1/16) and Pt(1/8) for the first 30 s. We attribute this instantaneous, large signal to the pseudocapacitive current from ruthenium oxides or oxyhydroxides. In potentiostatic experiments, current associated with electrochemical double-layer and pseudocapacitor behavior dominates faradaic reactions at the beginning of the experiments. The typical time constant for the electrochemical double-layer capacitor was 10^{-3} s; however, the pseudocapacitor behaviors of ruthenium oxides/oxyhydroxides are expected to persist much longer because of their notable pseudocapacitance. Among our samples, the PtRu/C contained the largest number of Ru atoms on the PtRu surface as validated in the XAS and ECSA CV profiles. Therefore, its transient current became the largest, as expected. When the PtRu/C was fully poisoned after 10 min, it exhibited a steady current plateau without further degradation. With respect to Pt(1/16) and Pt(1/8), both samples exhibited significantly improved CO tolerance with larger MOR

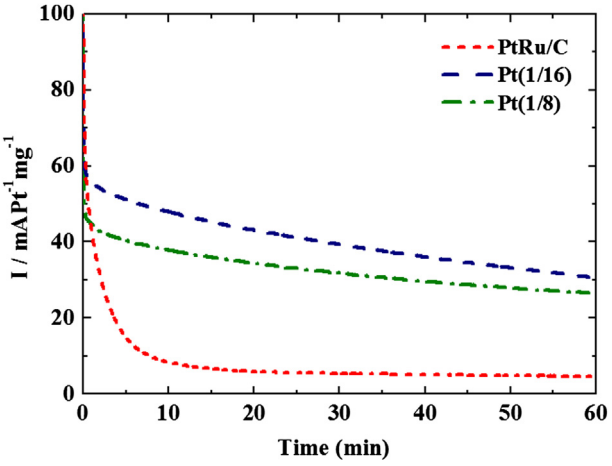

Fig. 9. The MOR chronoamperograms for PtRu/C, Pt(1/16), and Pt(1/8). The electrolyte is an aqueous solution of 0.5 M H_2SO_4 and 1 M CH_3OH, and the potential is fixed at 0.63 V (vs. RHE).

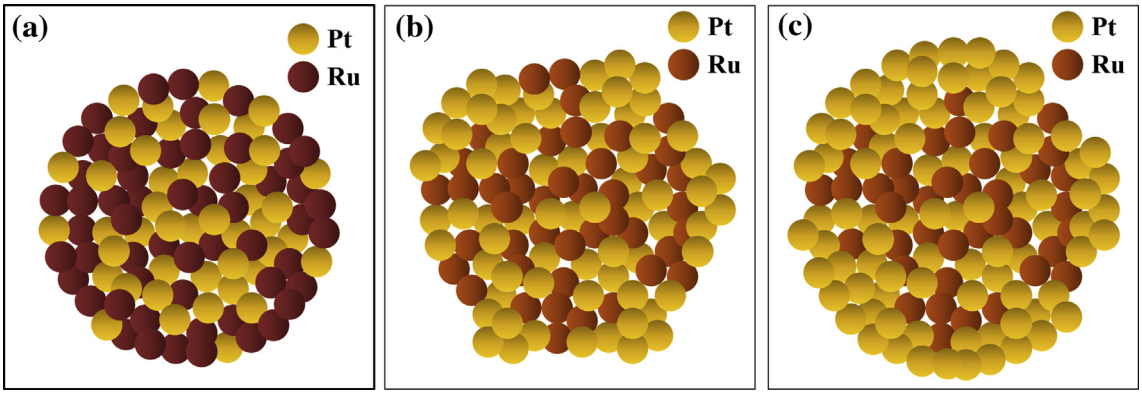

Fig. 10. Schematic illustrations of the surfaces of PtRu/C, Pt(1/16), and Pt(1/8).

currents. However, the poisoning effect was occurring gradually, so the current eventually drifted toward a steady current.

We understand that the severity of a displacement reaction plays a significant role in the surface composition and bonding structure for the resulting PtRu/C nanoparticles. XAS analyses of the Pt(1/16) and Pt(1/8) samples confirmed that Pt-rich surfaces were achieved. However, the ICP-MS results indicated that, the amount of Ru lost during surface modification was rather negligible. We also analyzed the Pt electrolyte after surface modification via ICP-MS analysis and found that the concentration of Pt ions was below the detection limit. Because sufficient amounts of Pt ions were present in the prepared samples to form monolayered Pt (for Pt(1/8) sample) and sub-monolayered Pt (for Pt(1/16) sample), we realized that the surface modification treatment was successfully achieved and that the surface became enriched with Pt in the order Pt(1/8) > Pt(1/16) > PtRu/C. In addition, the electrochemical analysis of MOR activities and the chronoamperograms demonstrated consistent trends. In summary, results from XRD, TEM, ICP-MS, XAS, and electrochemical measurements provide a coherent picture and the postulated schematics for our sample surfaces are depicted in Fig. 10.

Our method provides a facile surface modification route to improve the electrocatalytic properties of commercial PtRu nanoparticles. According to the literature, PtRu nanoparticles have been generally accepted as exhibiting the highest MOR activities. However, the Pt:Ru ratio of 1:1 is nominal at best because the Pt and Ru atoms have distinct chemical affinities; therefore, the exact surface Pt/Ru ratios and their distribution states are contingent on the involved synthesis and post-treatments. Hence, the optimized surface PtRu composition is still under debate. Earlier, Liu et al. used X-ray absorption spectroscopy to analyze commercial PtRu nanoparticles from both E-TEK and Johnson Matthey [44]. They determined that both samples were Pt rich at their cores and Ru rich in their shells. In a similar work, Hwang et al. performed H_2 reduction treatments on PtRu nanoparticles from Johnson Matthey and produced a Pt-rich surface with significantly enhanced activities for MOR and improved CO tolerance [22]. Our results are consistent with their findings because the displacement reaction between the Pt ions in the electrolyte and the Ru atoms on the PtRu surface renders a modified surface with excess Pt deposited. This excess Pt leads to a Pt-enriched surface as indicated by our XAS profiles, improved MOR and increased CO tolerance.

4. Conclusions

We successfully deposited Pt atoms on commercially available PtRu/C by initiating a displacement reaction between the Ru atoms on the surface of PtRu/C and the Pt ions in an aqueous hexachloroplatinic acid electrolyte. The hexachloroplatinic acid concentration was deliberately formulated to allow for the formation of sub-monolayered and monolayered Pt; therefore, after the displacement reaction, the PtRu/C nanoparticles exhibited Pt-enriched surfaces. The XRD and TEM results showed identical phases with a slight increase in the PtRu sizes. ICP-MS confirmed Pt deposition with negligible loss of Ru mass, thereby indicating that a cementation reaction was involved. XAS spectra from XAS suggested that the surface was enriched with Pt in the order Pt(1/8) > Pt(1/16) > PtRu/C. Electrochemical measurements in the form of CVs and chronoamperograms for MOR activities showed that Pt(1/16) exhibited better catalytic ability and better carbon monoxide tolerance, followed by Pt(1/8) and PtRu/C. With respect to mass activities, the Pt(1/16) showed a 223% increase over that of PtRu/C; this increase was attributed to the reduced Ru ratio on the PtRu surface.

Acknowledgments

Financial supports from National Science Council (NSC100-2221-E009-075-MY3) and National Synchrotron Radiation Research Center are greatly appreciated.

References

[1] G.J.K. Acres, J. Power Sources 100 (2001) 60–66.
[2] K.M. McGrath, G.K.S. Prakash, G.A. Olah, J. Ind. Eng. Chem. 10 (2004) 1063–1080.
[3] V. Neburchilov, J. Martin, H.J. Wang, J.J. Zhang, J. Power Sources 169 (2007) 221–238.
[4] J.H. Wee, J. Power Sources 173 (2007) 424–436.
[5] K.Y. Chan, J. Ding, J.W. Ren, S.A. Cheng, K.Y. Tsang, J. Mater. Chem. 14 (2004) 505–516.
[6] C.W. Yang, X.G. Hu, D.L. Wang, C.S. Dai, L. Zhang, H.B. Jin, S. Agathopoulos, J. Power Sources 160 (2006) 187–193.
[7] A.N. Gavrilov, E.R. Savinova, P.A. Simonov, V.I. Zaikovskii, S.V. Cherepanova, G.A. Tsirlina, V.N. Parmon, Phys. Chem. Chem. Phys. 9 (2007) 5476–5489.
[8] P. Waszczuk, G.Q. Lu, A. Wieckowski, C. Lu, C. Rice, R.I. Masel, Electrochim. Acta 47 (2002) 3637–3652.
[9] T. Yajima, H. Uchida, M. Watanabe, J. Phys. Chem. B 108 (2004) 2654–2659.
[10] S. Alayoglu, A.U. Nilekar, M. Mavrikakis, B. Eichhorn, Nat. Mater. 7 (2008) 333–338.
[11] Y. Kang, L. Qi, M. Li, R.E. Diaz, D. Su, R.R. Azic, E. Stach, J. Li, C.B. Murray, ACS Nano 3 (2012) 2818–2825.
[12] T. Frelink, W. Visscher, J. Van Veen, Surf. Sci. 335 (1995) 353–360.
[13] R.R. Adzic, J. Zhang, K. Sasaki, M.B. Vukmirovic, M. Shao, J.X. Wang, A.U. Nilekar, M. Mavrikakis, J.A. Valerio, F. Uribe, Top. Catal. 46 (2007) 249–262.
[14] H. Miura, T. Suzuki, Y. Ushikubo, K. Sugiyama, T. Matsuda, R.D. Gonzalez, J. Catal. 85 (1984) 331–338.
[15] W. Wang, R.F. Wang, H. Wang, S. Ji, J. Key, X.Z. Li, Z.Q. Lei, J. Power Sources 196 (2011) 9346–9351.

[16] C.H. Chen, L.S. Sarma, D.Y. Wang, F.J. Lai, C.C. Al Andra, S.H. Chang, D.G. Liu, C.C. Chen, J.F. Lee, B.J. Hwang, ChemCatChem 2 (2010) 159–166.
[17] L. Dubau, C. Coutanceau, E. Garnier, J.M. Léger, C. Lamy, J. Appl. Electrochem. 33 (2003) 419–429.
[18] Y.C. Hsieh, P.W. Wu, Y.J. Lu, Y.M. Chang, J. Electrochem. Soc. 156 (2009) B735–B742.
[19] S.R. Brankovic, J. McBreen, R.R. Adžić, J. Electroanal. Chem. 503 (2001) 99–104.
[20] E.V. Spinacé, A.O. Neto, M. Linardi, J. Power Sources 129 (2004) 121–126.
[21] Y.C. Hsieh, L.C. Chang, P.W. Wu, Y.M. Chang, J.F. Lee, Appl. Catal. B 103 (2011) 116–127.
[22] B.J. Hwang, L.S. Sarma, G.R. Wang, C.H. Chen, D.G. Liu, H.S. Sheu, J.F. Lee, Chem. Eur. J. 13 (2007) 6255–6264.
[23] X. Li, J. Liu, Q. Huang, W. Vogel, D.L. Akins, H. Yang, Electrochim. Acta 56 (2010) 278–284.
[24] S. Stoupin, E.H. Chung, S. Chattopadhyay, C.U. Segre, E.S. Smotkin, J. Phys. Chem. B 110 (2006) 9932–9938.
[25] R. Viswanathan, G. Hou, R. Liu, S.R. Bare, F. Modica, G. Mickelson, C.U. Segre, N. Leyarovska, E.S. Smotkin, J. Phys. Chem. B 106 (2002) 3458–3465.
[26] W.E. O'Grady, P.L. Hagans, K.I. Pandya, D.L. Maricle, Langmuir 17 (2001) 3047–3050.
[27] J. McBreen, S. Mukerjee, J. Electrochem. Soc. 142 (1995) 3399–3404.
[28] B.J. Hwang, L.S. Sarma, J.M. Chen, C.H. Chen, S.C. Shih, G.R. Wang, D.G. Liu, J.F. Lee, M.T. Tang, J. Am. Chem. Soc. 127 (2005) 11140–11145.
[29] N. Takeno, Geological Survey of Japan Open File Report, 2005, p. 102.
[30] S.R. Brankovic, J.X. Wang, R.R. Adžić, Electrochem. Solid State Lett. 4 (2001) A217–A220.
[31] D. Michell, D.A.J. Rand, R. Woods, J. Electroanal. Chem. 89 (1978) 11–27.
[32] S.Y. Huang, S.M. Chang, C.L. Lin, C.H. Chen, C.T. Yeh, J. Phys. Chem. B 110 (2006) 23300–23305.
[33] J.X. Wang, H. Inada, L. Wu, Y. Zhu, Y. Choi, P. Liu, W.P. Zhou, R.R. Adzic, J. Am. Chem. Soc. 131 (2009) 17298–17302.
[34] T. Iwasita, H. Hoster, A. John-Anacker, W.F. Lin, W. Vielstich, Langmuir 16 (2000) 522–529.
[35] C.C. Wang, C.C. Hu, Carbon 43 (2005) 1926–1935.
[36] C.F. Tsai, K.Y. Yeh, P.W. Wu, Y.F. Hsieh, P. Lin, J. Alloys Compd. 478 (2009) 868–871.
[37] D. Chu, S. Gilman, J. Electrochem. Soc. 143 (1996) 1685–1690.
[38] A.S. Aricò, P.L. Antonucci, E. Modica, V. Baglio, H. Kim, V. Antonucci, Electrochim. Acta 47 (2002) 3723–3732.
[39] H.A. Gasteiger, N. Markovic, P.N. Ross, E.J. Cairns, J. Phys. Chem. 97 (1993) 12020–12029.
[40] H.A. Gasteiger, N. Marković, P.N. Ross Jr., E.J. Cairns, Electrochim. Acta 39 (1994) 1825–1832.
[41] F. Maillard, F. Gloaguen, J.M. Leger, J. Appl. Electrochem. 33 (2003) 1–8.
[42] J.H. Ma, Y.Y. Feng, J. Yu, D. Zhao, A.J. Wang, B.Q. Xu, J. Catal. 275 (2010) 34–44.
[43] Y.C. Hsieh, J.Y. Chen, P.W. Wu, J. Power Sources 196 (2011) 8225–8233.
[44] D.G. Liu, J.F. Lee, M.T. Tang, J. Mol. Catal. A: Chem. 240 (2005) 197–206.